



Contents lists available at ScienceDirect

Computers & Fluids

journal homepage: www.elsevier.com/locate/compfluid

High-order accurate simulations of unsteady flow past plunging and pitching airfoils

Chunlei Liang^{a,*}, Kui Ou^b, Sachin Premasuthan^b, Antony Jameson^b, Z.J. Wang^c^a Department of Mechanical and Aerospace Engineering, George Washington University, Washington, DC 20052, United States^b Aeronautics and Astronautics, Stanford University, Stanford, CA 94305, United States^c Department of Aerospace Engineering, Iowa State University, Ames, IA 50011, United States

ARTICLE INFO

Article history:

Received 5 October 2009

Received in revised form 9 June 2010

Accepted 8 September 2010

Available online xxxxx

Keywords:

Spectral difference method

Plunging

Pitching

Micro Air Vehicle

ABSTRACT

This paper presents simulations of unsteady flow past plunging and pitching airfoils using a high-order spectral difference (SD) method. Both third-order and fourth-order SD methods are employed on unstructured quadrilateral grids for the plunging airfoil at a low Reynolds number. The vortex shedding pattern of an airfoil in an oscillating plunge motion becomes asymmetric at a sufficiently high frequency. The SD method is able to capture this effect and reveal a fine structure that closely replicates the experimental photograph. Interestingly, our simulations also predict that the degree of this asymmetry increases with Reynolds number. Unsteady flow at a higher Reynolds number past a pitching airfoil is studied using the fifth-order SD method. Our predictions show very good agreements with the available experimental data. The developed high-order accurate SD algorithms could enable high-order accurate simulations of unsteady flow past flapping Micro-Air-Vehicles (MAVs).

Published by Elsevier Ltd.

1. Introduction

Increases in computational power are enabling high-order accurate simulations of various research problems previously deemed intractable such as unsteady Large Eddy Simulation (LES), Aeroacoustics and fluid-structure interaction. The need for highly accurate methods in these applications on complex geometries has seen the development of higher order schemes for unstructured meshes such as the Discontinuous Galerkin (DG) Method [1], Spectral Volume (SV) method [13,26] and Spectral Difference (SD) Method [12,25]. The SD method is a recently developed efficient high-order approach based on the differential form of the governing equation. It was originally proposed by Kopriva and Koliás [7]. A general formulation was given by Liu et al. [12], who developed the method for wave equations on triangular grids. Wang et al. [25] extended it to 2D Euler equations on triangular grids and [22] further developed it for three-dimensional Navier–Stokes equations on hexahedral unstructured meshes. The SD method combines elements from finite-volume and finite-difference techniques. The method is particularly attractive because it is conservative, has a simple formulation and is easy to implement. The conservative property of the SD scheme was discussed in Wang et al. [25].

Lift is produced by steady flow over aircraft surfaces. In contrast, natural fliers create lift and thrust from unsteady aerodynamics by flapping and hovering their wings. Computing unsteady flows at low to moderate Reynolds number continues to be of significant interest due to its application in MAVs and its relevance to insect

and bird flight. Flapping flight of birds and insects are fine examples of highly efficient motion of aerodynamic surfaces that simultaneously develop the necessary thrust for forward motion and sustained lift force for remaining airborne. Because of the abrupt nature of the vortex formation and breakdown and their extreme sensitivity to plunging/pitching amplitude and frequency, a high-order accurate simulation is very desirable in order to minimize the numerical dissipation which often prevents accurate prediction of the energy and location of vortices as well as their life cycle.

In addition, the oscillating wing devices using hybrid plunging and pitching motion, have been demonstrated as a potentially more efficient concept to harness wind [14] and tidal energy [18] than conventional energy harvesting systems with rotational blades. Kinsey and Dumas [5] reported that for their sinusoidal cases studied, where high power coefficients were generated, the plunging contribution to power largely dominated the pitching contribution. They concluded that generation of leading edge vortices aided synchronization between the airfoil velocity and the translational force for as long as possible through the flapping cycle, a condition necessary for high power generation. Platzer et al. [18] implemented their idea that the airfoil plunge is maintained for as long as possible at a high velocity, followed by rapid pitching reversals. They demonstrated that non-sinusoidal pitch-plunge motion produces 30% increase in power generation.

Oscillating wing devices commonly produce vortex dominated unsteady flow. As a result, schemes with low numerical dissipation on moving grids are desirable in order to perform accurate simulations. In this paper, we report our further developments of the high-order SD method for these moving boundary unsteady flow problems. We study plunging and pitching motions separately

* Corresponding author. Tel.: +1 202 994 7073.

E-mail address: chliang@gwu.edu (C. Liang).

in order to understand their individual impacts on airfoil performance.

For remaining parts of this paper, we present numerical formulation of the SD method in Section 2. In Section 3, we verify the accuracy of our method using a 2D viscous flow Taylor–Couette flow problem. The major results for unsteady flow past an airfoil are presented in Section 4. Finally, conclusions are drawn in Section 5.

2. Numerical formulation

We have reported the baseline 2D code development for solving Navier–Stokes equations on fixed grids in Liang et al. [11,9].

2.1. Discretization in 2D space

Consider the unsteady 2D conservation law of the form

$$\frac{\partial Q}{\partial t} + \frac{\partial F}{\partial x} + \frac{\partial G}{\partial y} = 0 \quad (1)$$

where Q is the vector of conserved variables; F and G are the total fluxes including both inviscid and viscous flux vectors. To achieve an efficient implementation, all elements in the physical domain (x, y) are transformed into a standard square element $(0 \leq \xi \leq 1, 0 \leq \eta \leq 1)$ as shown in Fig. 1. The transformation can be written as:

$$\begin{pmatrix} x \\ y \end{pmatrix} = \sum_{i=1}^K M_i(\xi, \eta) \begin{pmatrix} x_i \\ y_i \end{pmatrix} \quad (2)$$

where K is the number of points used to define the physical element, (x_i, y_i) are the cartesian coordinates of those points, and $M_i(\xi, \eta)$ are the shape functions. The metrics and the Jacobian of the transformation can be computed. The governing equations in the physical domain are then transferred into the computational domain, and the transformed equations take the following form:

$$\frac{\partial \tilde{Q}}{\partial t} + \frac{\partial \tilde{F}}{\partial \xi} + \frac{\partial \tilde{G}}{\partial \eta} = 0 \quad (3)$$

where $\tilde{Q} = |J| \cdot Q$ and

$$\begin{pmatrix} \tilde{F} \\ \tilde{G} \end{pmatrix} = |J| \begin{pmatrix} \xi_x \xi_y \\ \eta_x \eta_y \end{pmatrix} \begin{pmatrix} F \\ G \end{pmatrix} \quad (4)$$

In the standard element, two sets of points are defined, namely the solution points and the flux points, illustrated in Fig. 1. In order to construct a degree $(N - 1)$ polynomial in each coordinate direction, solution at N points are required. The solution points in 1D are chosen to be the Gauss points defined by:

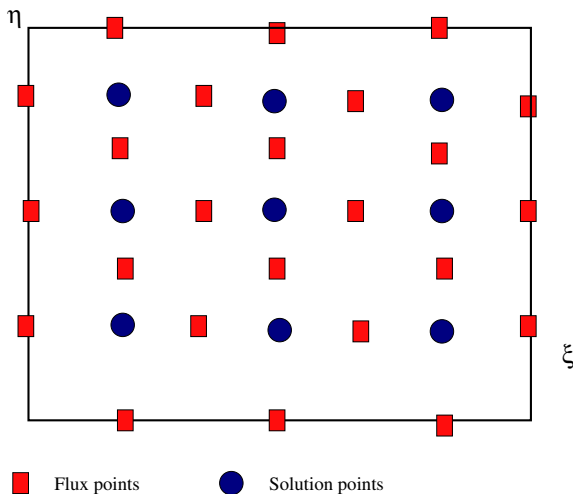


Fig. 1. Distribution of flux and solution points for the third-order SD scheme.

$$X_s = \frac{1}{2} \left[1 - \cos \left(\frac{2s-1}{2N} \cdot \pi \right) \right], \quad s = 1, 2, \dots, N. \quad (5)$$

The flux points are selected as Legendre–Gauss–quadrature points plus two end points as suggested by Huynh [3] and Van den Abeele et al. [23].

Using the solutions at N solution points, a degree $(N - 1)$ polynomial can be built using the following Lagrange basis defined as:

$$h_i(X) = \prod_{s=0, s \neq i}^N \left(\frac{X - X_s}{X_i - X_s} \right) \quad (6)$$

Similarly, using the fluxes at $(N + 1)$ flux points, a degree N polynomial can be built for the flux using a similar Lagrange basis defined as:

$$l_{i+1/2}(X) = \prod_{s=0, s \neq i}^N \left(\frac{X - X_{s+1/2}}{X_{i+1/2} - X_{s+1/2}} \right) \quad (7)$$

For instance, for a second-order scheme, the first basis is defined as

$$l_{1/2}(X) = \frac{X - X_{1+1/2}}{X_{1/2} - X_{1+1/2}} \frac{X - X_{2+1/2}}{X_{1/2} - X_{2+1/2}} \quad (8)$$

The reconstructed solution for the conserved variables in the standard element is just the tensor products of the two one-dimensional polynomials,

$$Q(\xi, \eta) = \sum_{j=1}^N \sum_{i=1}^N \frac{\tilde{Q}_{ij}}{|J_{ij}|} h_i(\xi) \cdot h_j(\eta) \quad (9)$$

Similarly, the reconstructed flux polynomials take the following form:

$$\begin{aligned} \tilde{F}(\xi, \eta) &= \sum_{j=1}^N \sum_{i=0}^N \tilde{F}_{i+1/2, j} l_{i+1/2}(\xi) \cdot h_j(\eta), \\ \tilde{G}(\xi, \eta) &= \sum_{j=0}^N \sum_{i=1}^N \tilde{G}_{i, j+1/2} h_i(\xi) \cdot l_{j+1/2}(\eta) \end{aligned} \quad (10)$$

These reconstructed fluxes are only element-wise continuous, but discontinuous across cell interfaces. For the inviscid flux, a Riemann solver is employed to compute a common flux at interfaces to ensure conservation and stability. In our case, we have used both the Rusanov solver [20] and the Roe solver [19] to compute the interface fluxes.

In summary, the algorithm to compute the inviscid flux derivatives consists of the following steps:

- Given the conservative variables at the solution points, the conservative variables are computed at the flux points and the inviscid fluxes at the interior flux points can be determined.
- The inviscid fluxes at the element interfaces are computed using the Riemann solver. Given the normal direction of the interface n , and the averaged normal velocity component V_n and the sound speed c , the inviscid flux on the interface can be determined.
- The derivatives of the fluxes are computed at the solution points using the derivatives of Lagrange operators l

$$\begin{aligned} \left(\frac{\partial \tilde{F}}{\partial \xi} \right)_{ij} &= \sum_{r=0}^N \tilde{F}_{r+1/2, j} \cdot l'_{r+1/2}(\xi_i), \\ \left(\frac{\partial \tilde{G}}{\partial \eta} \right)_{ij} &= \sum_{r=0}^N \tilde{G}_{i, r+1/2} \cdot l'_{r+1/2}(\eta_j) \end{aligned} \quad (11)$$

To illustrate the treatment of viscous flows, one can write the two-dimensional Navier–Stokes equations in conservation form as

$$\frac{\partial Q}{\partial t} + \nabla \mathbf{F}_{inv}(Q) - \nabla \mathbf{F}_{vis}(Q, \nabla Q) = 0 \quad (12)$$

where the conservative variables Q and Cartesian components $f_e(Q)$ and $g_e(Q)$ of the inviscid flux vector $\mathbf{F}_{inv}(Q)$ are given by

$$Q = \begin{Bmatrix} \rho \\ \rho u \\ \rho v \\ E \end{Bmatrix}, f_{inv}(Q) = \begin{Bmatrix} \rho u \\ \rho u^2 + p \\ \rho uv \\ u(E + p) \end{Bmatrix}, g_{inv}(Q) = \begin{Bmatrix} \rho v \\ \rho uv \\ \rho v^2 + p \\ v(E + p) \end{Bmatrix} \quad (13)$$

Here ρ is the density, u and v are the velocity components in x and y directions, p stands for pressure and E is the total energy. The pressure is related to the total energy by

$$E = \frac{p}{\gamma - 1} + \frac{1}{2} \rho (u^2 + v^2) \quad (14)$$

with a constant ratio of specific heats γ . For all test cases in the present study, γ is set as 1.4 for air.

The Cartesian components $f_{vis}(Q, \nabla Q)$ and $g_{vis}(Q, \nabla Q)$ of the viscous flux vector $\mathbf{F}_{vis}(Q, \nabla Q)$ are given by

$$f_{vis}(Q, \nabla Q) = \mu \begin{Bmatrix} 0 \\ 2u_x + \lambda(u_x + v_y) \\ v_x + u_y \\ u[2u_x + \lambda(u_x + v_y)] + v(v_x + u_y) + \frac{C_p}{Pr} T_x \end{Bmatrix}$$

$$g_{vis}(Q, \nabla Q) = \mu \begin{Bmatrix} 0 \\ v_x + u_y \\ 2v_y + \lambda(u_x + v_y) \\ v[2v_y + \lambda(u_x + v_y)] + u(v_x + u_y) + \frac{C_p}{Pr} T_y \end{Bmatrix} \quad (15)$$

where μ is the dynamic viscosity, C_p is the specific heat and Pr stands for Prandtl number. T is temperature which can be derived from the perfect gas assumption. λ is set to $-2/3$ according to the Stokes hypothesis.

The procedures to get the viscous fluxes can be described as the following steps:

- (1) reconstruct Q_f at the flux points from the conservative variables at the solution points using Eq. (9).
- (2) average the field of Q_f on the element interfaces as $\overline{Q}_f = \frac{1}{2} (Q_f^L + Q_f^R)$. For interior flux points, $\overline{Q}_f = Q_f$. Meanwhile, appropriate boundary conditions shall be applied for specific boundary flux points.
- (3) evaluate ∇Q at solution points from \overline{Q}_f using Eq. (11) where $\nabla Q = \begin{Bmatrix} Q_x \\ Q_y \end{Bmatrix}$ and $Q_x = \frac{\partial Q}{\partial \xi} \xi_x + \frac{\partial Q}{\partial \eta} \eta_x$, etc.
- (4) reconstruct ∇Q from solution points to flux points and using Eq. (9), average them on the element interfaces as $\overline{\nabla Q}_f = \frac{1}{2} (\nabla Q_f^L + \nabla Q_f^R)$
- (5) use \overline{Q}_f and $\overline{\nabla Q}_f$ in order to compute the viscous flux vectors described in Eq. (15) at the element interfaces.

2.2. Extension of the SD method to moving and deformable grids

Morton et al. [16] and Persson et al. [17] have shown that the Navier–Stokes equations on moving and deformable grids can be transformed using a mapping technique to a stationary structured and unstructured grids respectively.

Let \mathcal{M} denote a time-dependent continuous mapping function from a reference domain $(X, Y)_{t0}$ to a physical domain $(x, y)_t$ such that $(x, y) = \mathcal{M}(X, Y, t)$. The mapping gradient is $\mathbf{G} = \nabla_X \mathcal{M} = \frac{\partial(x, y)}{\partial(X, Y)}$. The determinant of the mapping is the Jacobian g . The mapping velocity \mathbf{w} can be determined from the time derivative of \mathcal{M} .

The conservative Eq. (12) on the physical (moving and deformable) domain can be re-written as

$$\frac{\partial \hat{Q}}{\partial t} \Big|_x + \nabla_X \hat{\mathbf{F}}_{inv}(\hat{Q}) - \nabla \hat{\mathbf{F}}_{vis}(\hat{Q}, \nabla \hat{Q}) = 0 \quad (16)$$

where $\hat{Q} = gQ$, $\hat{\mathbf{F}}_{inv} = g\mathbf{G}^{-1}\mathbf{F}_{inv} - \mathbf{G}^{-1}\mathbf{w}\hat{Q}$ and $\hat{\mathbf{F}}_{vis} = g\mathbf{G}^{-1}\mathbf{F}_{vis}$. The gradient of conservative variables on the physical domain can be simply expressed on the reference domain using a chain rule

$$\nabla Q = \nabla_X (g^{-1} \hat{Q}) \partial X / \partial x = [g^{-1} \nabla_X \hat{Q} + \hat{Q} \nabla_X (g^{-1})] \mathbf{G}^{-T} \quad (17)$$

The high-order method can then be applied directly to the transformed equations on the stationary grids. Implementing the geometric conservation law correction term for g is also expected to make our algorithms more robust for large deformations. Nevertheless, since we only consider plunge/pitch motion without mesh deformation in this paper, a simplification can be made as $g = 1$ for both cases. The transverse plunge motion is defined as a mapping function of $X = x$ and $Y(t) = y + h \cos(\omega t)$ globally for all mesh points. The pitching motion is defined as $X = \cos\theta \cdot x + \sin\theta \cdot y$ and $Y = -\sin\theta \cdot x + \cos\theta \cdot y$ for all mesh points, where $\theta = A \sin(2\pi f t)$ and A is pitching amplitude.

2.3. Time advancement schemes

Flows with either steady or unsteady solutions are considered in this paper. All computations utilize a fourth-order accurate, strong-stability-preserving five-stage explicit Runge–Kutta time stepping scheme [21].

3. Validation studies

3.1. Order verification using compressible Taylor–Couette flow

In this example, the numerical order of accuracy is validated against the analytical solution for the compressible Taylor–Couette flow. This test problem was taken from a recent paper presented by Michalak and Ollivier-Gooch [15].

The Reynolds number is 10 based on the tangential magnitude of the spinning velocity of the inner cylinder and its radius ($=1$). The temperature and pressure are prescribed for the inner cylinder giving a Mach number 0.5. The outer cylinder is fixed and an adiabatic wall boundary condition is employed. A grid with 24×2 cells is shown in Fig. 2. Two other finer grids are obtained using successive grid refinements in both directions. A steady solution of Mach number contour obtained by the SD method is shown in Fig. 2b. A cubic curved wall boundary is used for inner and outer cylinders. We obtained desired numerical order $L2$ accuracy of the y -component of the angular velocity as shown in Table 1. The maximum accuracy of fourth-order is demonstrated in the table. The explicit Runge–Kutta scheme becomes slow when the polynomial order is increased. However, the fifth-order and even higher accuracy can also be demonstrated using the implicit LU-SGS method and p-multigrid approach with a significantly shorter CPU time [10].

4. Simulation results

In this section, we study unsteady flow past an airfoil using unstructured grids. The initial mixed-element mesh is shown in Fig. 3 and the far-field distance is 20 chords. The initial grid consists of 1881 elements. The NACA0012 airfoil upper surface is formed using only 20 edges. This grid is denoted as ‘Mesh 1A’. To perform one-level h-refinement and treat solid boundaries using high-order curved representation, the airfoil surface curve was

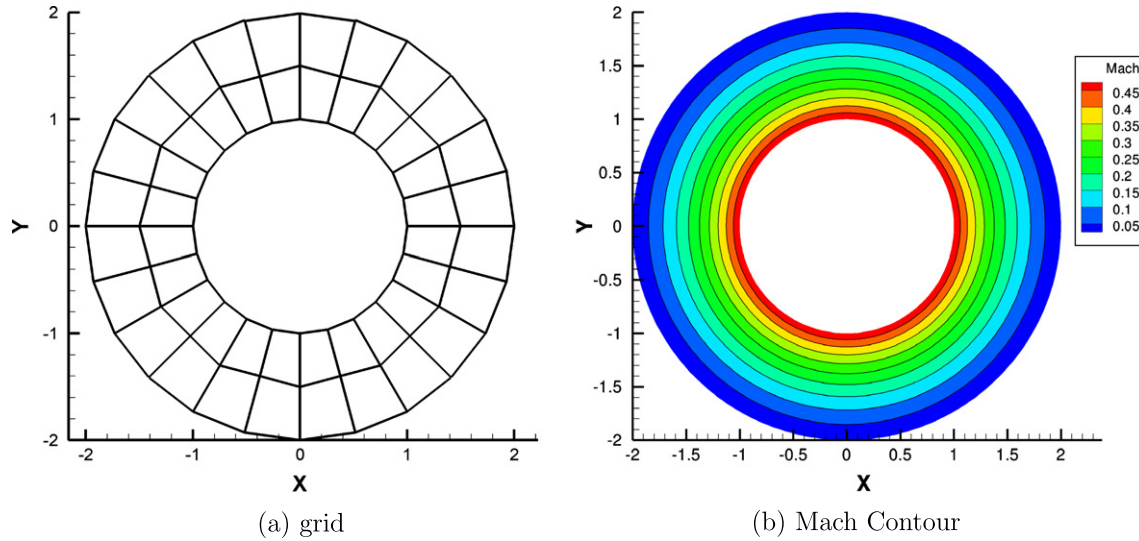


Fig. 2. Compressible Taylor-Couette Flow.

Table 1
 L^2 errors and orders of accuracy of viscous Taylor-Couette flow.

No. of elements	No. of DOFs	L2-error	Order
Third-order SD			
48	432	8.896E-04	-
192	1728	1.002E-04	3.15
768	6912	1.084E-05	3.21
Fourth-order SD			
48	768	1.4815E-04	-
192	3072	1.0036E-05	3.88
768	12,288	6.5746E-07	3.93

subdivided to match the domain of each edge on the surface of an existing mesh. After one-level h-refinement, a quadrilateral mesh with 5792 elements is obtained. A sectional part of this grid (Mesh 1B) is visualized in Fig. 4. Further details on the technique of h-refinement can be seen in Liang et al. [9]. In order to demonstrate the property of grid independence, a finer grid, namely Mesh 2B, is generated as shown in Fig. 5 with all triangular cells. The airfoil upper surface consists of 30 edges in Mesh 2A. We again perform

one-level h-refinement of Mesh 2A in order to obtain a finer mesh (Mesh 2B) to have 60 edges on the airfoil upper surface as shown in Figs. 6 and 7. If it is not mentioned elsewhere, the time step size of $\Delta t U_\infty/c = 2 \times 10^{-5}$ will be employed.

4.1. Viscous flow past a stationary NACA 0012 airfoil

Mesh 1B is used firstly for computing the flow past a stationary NACA 0012 airfoil. The inflow Mach number is 0.2 and the Reynolds number is 1850. Fig. 8 shows the pressure contour distribution obtained on Mesh 1B using a fourth-order SD method. The symmetry of pressure contour plot indicates that the viscous flow eventually settles with a steady flow solution. The drag coefficient predicted is 0.054.

Following the notation of Jones et al. [4], we define the plunge amplitude as h and plunge circular frequency as $\omega = 2\pi f$. Subsequently, the Strouhal number is determined as $Sr = \frac{\omega h c}{U_\infty}$, where c is the airfoil chord length and U_∞ is the free-stream velocity. The airfoil plunge motion profile considered in this paper is prescribed as $Y(t) = h \sin(\omega t)$. In the following, we consider two test problems, i.e. slow plunging airfoil and fast plunging airfoil.

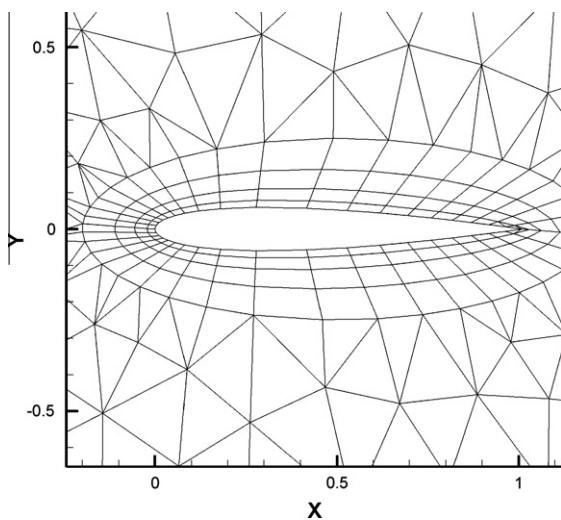


Fig. 3. Initial mixed-element mesh for NACA 0012 (Mesh 1A).

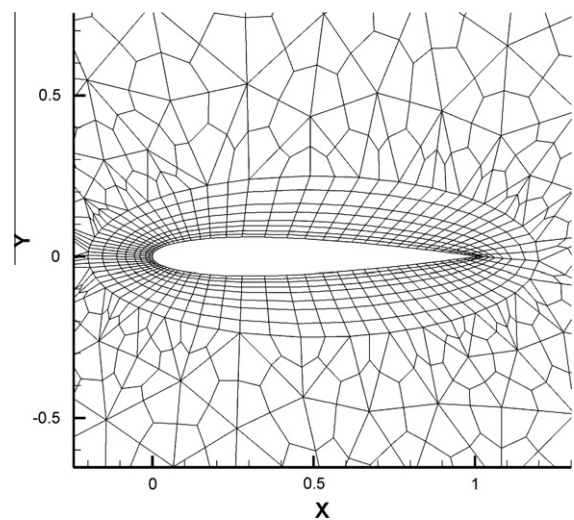


Fig. 4. Quadrilateral mesh after h-refinement for NACA 0012 (Mesh 1B).

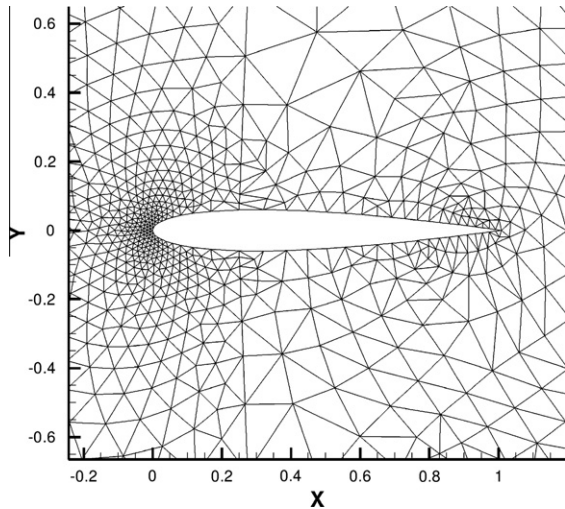


Fig. 5. A close view on the triangular cells in Mesh 2A.

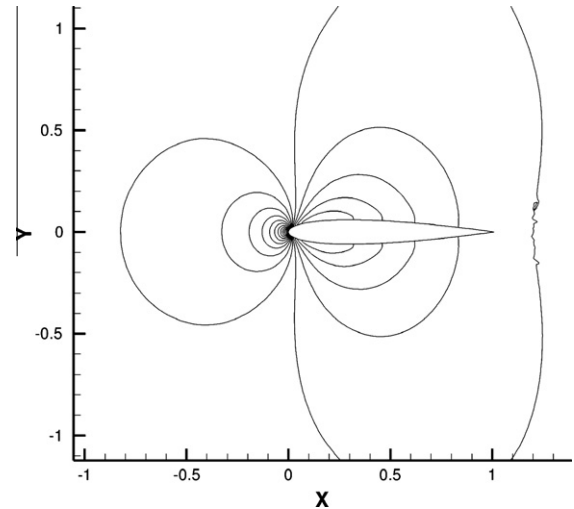


Fig. 8. The pressure contour plot obtained on Mesh 1B.

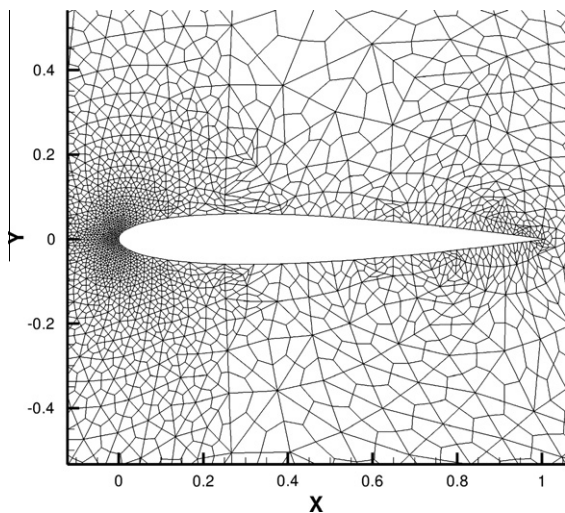


Fig. 6. A close view on the quadrilateral cells in Mesh 2B.

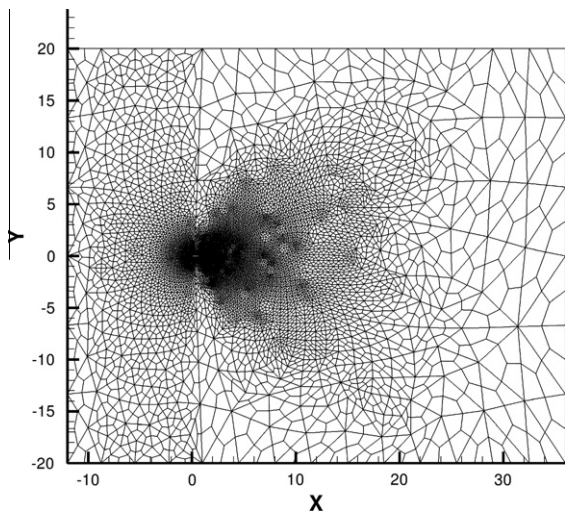


Fig. 7. Overall view of Mesh 2B.

4.2. Slow plunging airfoil

We consider a plunge motion with $\omega = 1.15$ and $h = 0.08c$. It corresponds to the test case with $Sr = 0.46$ in the paper of Jones et al [4]. We examine this slow plunging airfoil case using both the third-order and fourth-order SD methods on Mesh 1B. This flow has boundary layer separations from top and bottom sides which result in alternate vortex shedding patterns as shown in Fig. 9. The total 12 contour levels of $\omega c/U_\infty$ shown in Fig. 9 are bounded between -6 and 6 . In general, vortices are more confined by the fourth-order scheme than the third-order scheme. Fig. 9 also reveal that the numerical dissipation produced by the third-order scheme is significant after the seventh vortex. By analyzing the lift and drag coefficients for this slow plunging airfoil, we found that the vortex shedding frequency obtained from the lift coefficient (as shown in Fig. 10) is identical to the airfoil plunge motion frequency. The maximum of lift coefficients is around 4.77 and the minimum locates at the level of -0.042 . After discarding the initial transients for statistics, the overall time-averaged lift coefficient predicted is very close to zero (-0.0042). In contrast, the maximum drag coefficient predicted is 0.1 and the minimum drag reaches -0.181 . The overall time-averaged drag coefficient is negative (-0.0436). It can be summarized that the slow plunging airfoil under the above performance condition generates thrust but not lift.

In order to evaluate the effect of viscous stresses on this plunging airfoil, we compare computed lift and drag coefficients obtained by our SD viscous solver with the ones obtained by the inviscid Panel code employed in [4]. As shown in Fig. 11, the Panel code predicted a smaller magnitude of the lift coefficient and a considerably bigger magnitude of thrust force than that of the predictions by the SD solver.

4.3. Fast plunging airfoil

Finally, we consider the same airfoil with a plunge motion with $\omega = 2.46$ and $h = 0.12c$. This setup is identical to the one with $Sr = 1.5$ in the paper of Jones et al. [4]. The free-stream mach number is equivalent to the previous test case and maintained at the level of 0.2 using the Dirichlet boundary condition. As shown in Fig. 12a and b, our simulations suggest that the vortex shedding associated with a high-speed jet travels upwards with a degree of angle if the first stroke of the airfoil goes downwards, and vice versa. It shall be noted here that [2] observed that the high-speed jet switched to a different direction in their experiment at a much higher Reynolds number. We also noted that a numerical simula-

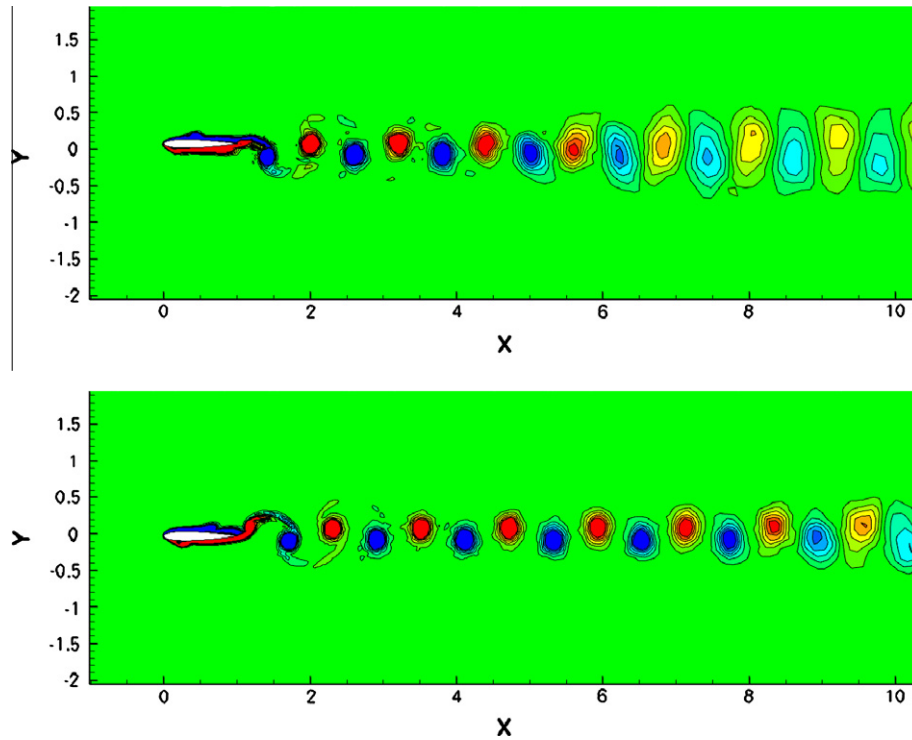


Fig. 9. The vorticity contour plot obtained using the third-order (top) and fourth-order (bottom) methods.

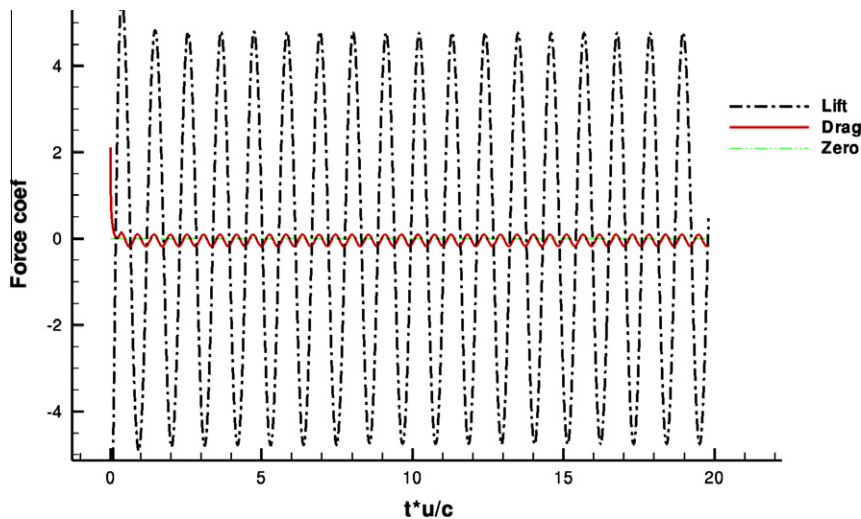


Fig. 10. The lift and drag coefficients obtained on Mesh 1B with the fourth-order SD method.

tion by Lewin and Haj-Hariri [8], which solved incompressible Navier–Stokes equations at Reynolds number of 500, predicted that their high-speed jet switched direction with either upward or downward angles.

The third-order SD method is able to reproduce the dual-mode vortex street as shown in Fig. 12a and b. They agree well with the experimental results shown in Fig. 12d obtained in a water tunnel. Using the same computational grid, the fourth-order SD method is able to reproduce the fine structures traveling in the opposite direction in the wake of the airfoil as shown in Fig. 12c. These fine structures resemble the structures shown in the photograph of the experiment by Jones et al. [4] and have not previously been reproduced in numerical simulations.

The lift and drag coefficients predicted by the third-order SD method shown on both Mesh 1B and Mesh 2B in Fig. 13 demonstrate that the solution is close to the state of grid independence. The difference between lift coefficients predicted Meshes 1B and 2B is negligible although there is a small difference between drag coefficients predicted by both meshes. The fourth-order SD scheme on Mesh 1B predicts that the time-averaged lift and drag coefficients are 2.57 and -0.51 respectively. The maximum instantaneous thrust is generated at the level of $C_d = -1.51$ in comparison to the maximum instantaneous drag of only around $C_d = 0.37$. Similar to the case with slow plunging motion, the dominant frequency obtained from the lift coefficient spectra is also equivalent to the plunge motion frequency.

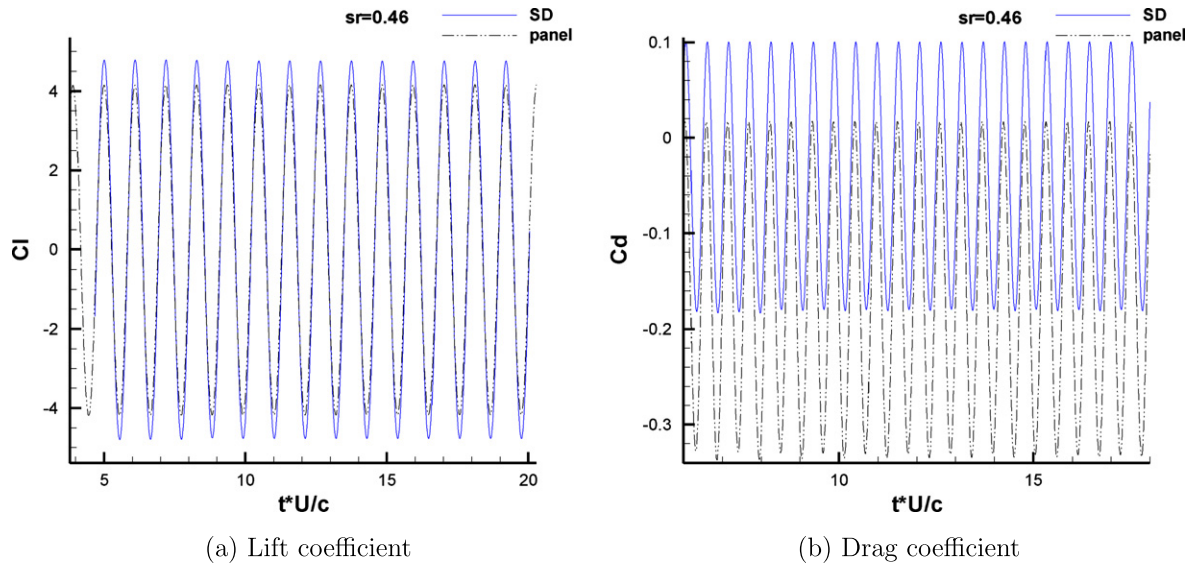


Fig. 11. Force coefficients obtained by SD and Panel codes.

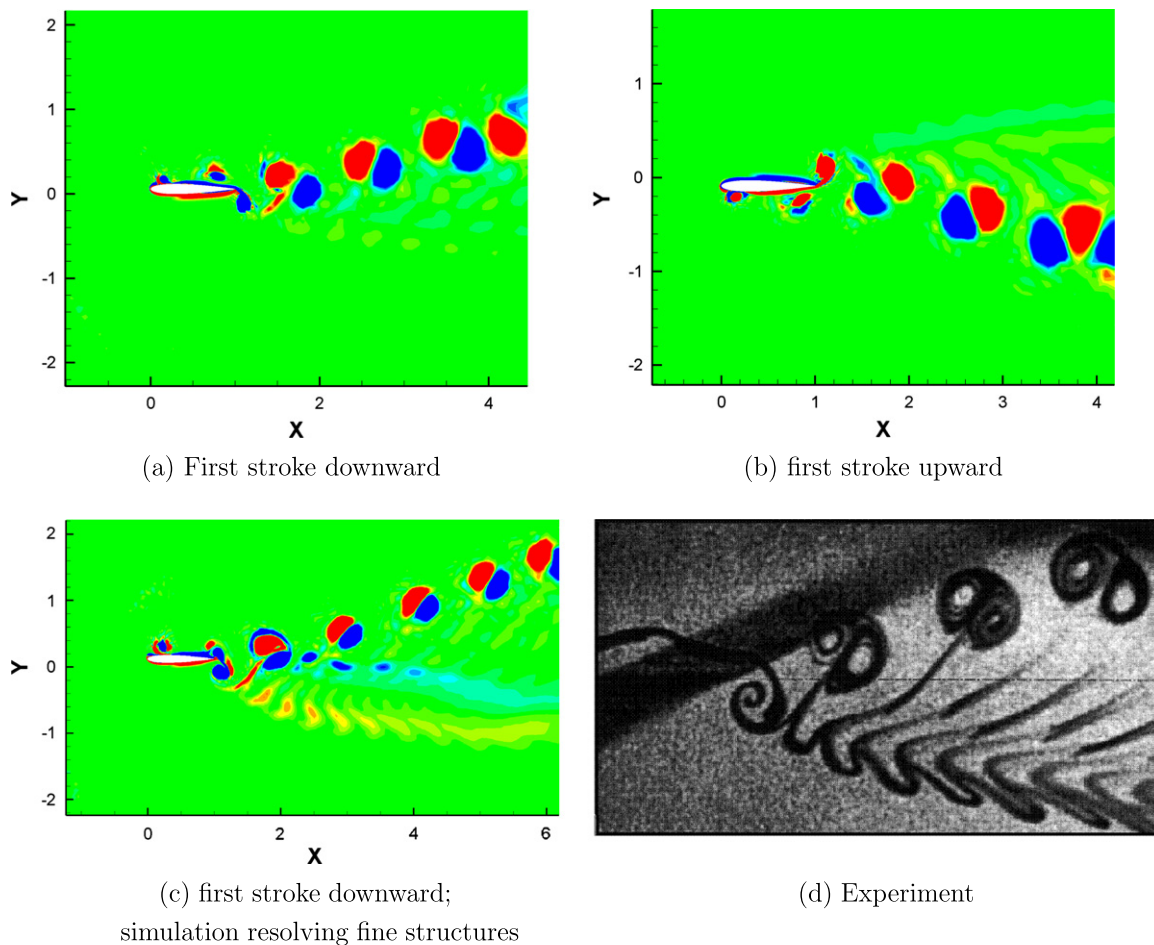


Fig. 12. The vorticity field predicted by the SD method against the experimental results presented in Jones et al. [4] and the contour levels are within the range of $-6 \leq \omega c / U_\infty \leq 6$. Both (a) and (b) are obtained by the third-order SD method, and (c) is obtained by the fourth-order SD method.

Once again, in order to evaluate the effect of viscous stresses on the plunging airfoil, in Fig. 14, we compare computed lift and drag coefficients obtained by our SD viscous code with the ones obtained by the inviscid Panel code employed in [4]. Both codes

compute the same plunge motion. The differences of lift coefficients predicted by both codes are very small. As the transverse plunge velocity increases, the dynamic pressure difference between top and bottom surfaces becomes more and more dominant and the

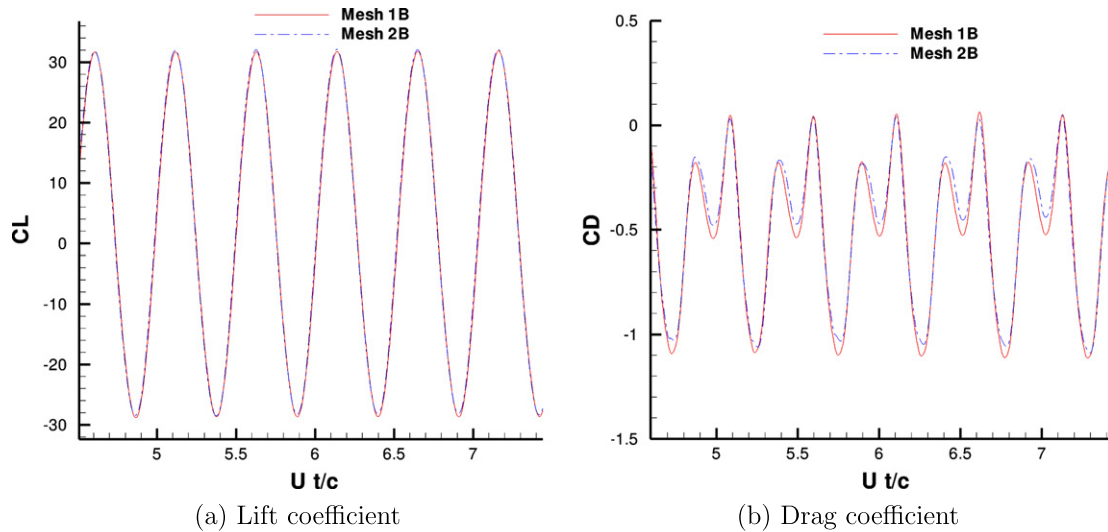


Fig. 13. Lift and drag coefficients predicted by Meshes 1B and 2B using third-order SD method.

difference of viscous stresses on top and bottom surfaces becomes negligible. However, viscous stresses win over pressure in the streamwise direction. The resultant thrust force predicted by the SD code has a peak magnitude only 30% as big as the peak magnitude predicted the Panel code.

The SD method worked well with the refined grid (Mesh 1B) as reported above. In order to demonstrate the grid-independence of our simulation results, two-level h-refinements are performed for the initial hybrid mesh (Mesh 1A). The final grid is shown in Fig. 15. This mesh is defined as 'Mesh 1C'. Mesh 1C has 23,168 grid points, which are 16 times the number of Mesh 1A.

In order to see the h-refinement effect on our simulation results, Mesh 1C is also used for the third-order SD simulation. Fig. 16 presents the vorticity contour plot. The contour levels are within the range of $-6 \leq \omega c/U_\infty \leq 6$. The third-order SD scheme on Mesh 1C is able to capture some fine structures in the downstream below the airfoil which were not resolved on Mesh 1B. However, the third-order SD scheme on Mesh 1C does not resolve these fine structures as clearly as the fourth-order SD scheme on Mesh 1B. It demonstrates that the p refinement is more effective than the h-refinement.

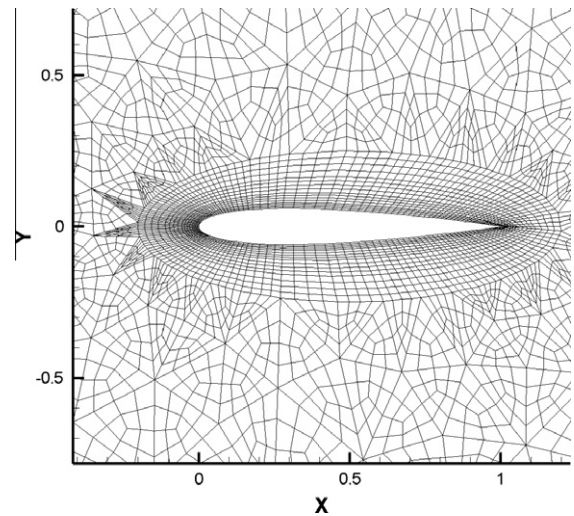


Fig. 15. All-quadrilateral-element mesh after two-level h-refinements (Mesh 1C).

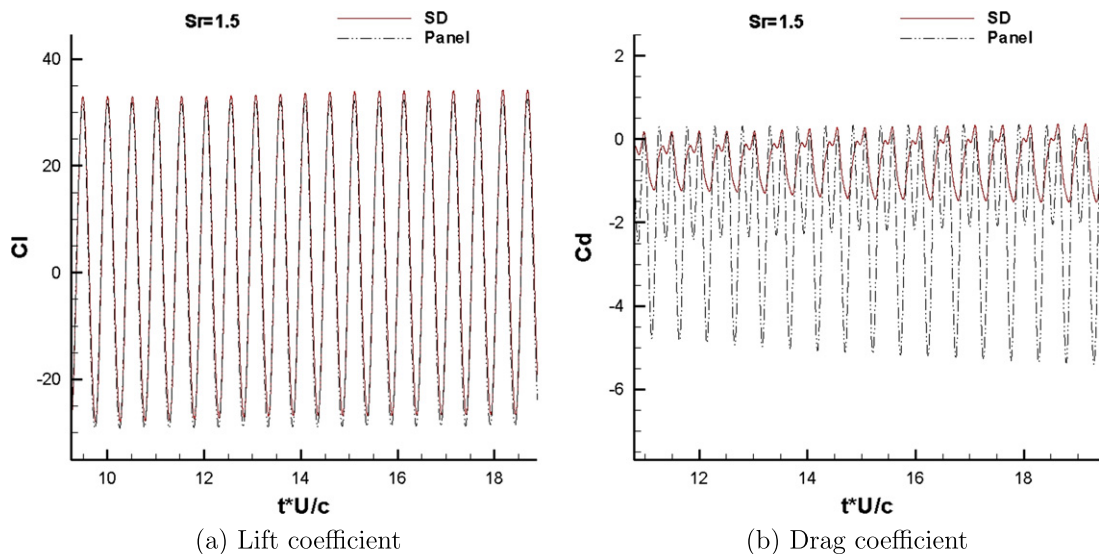


Fig. 14. Force coefficients obtained by SD and Panel codes.

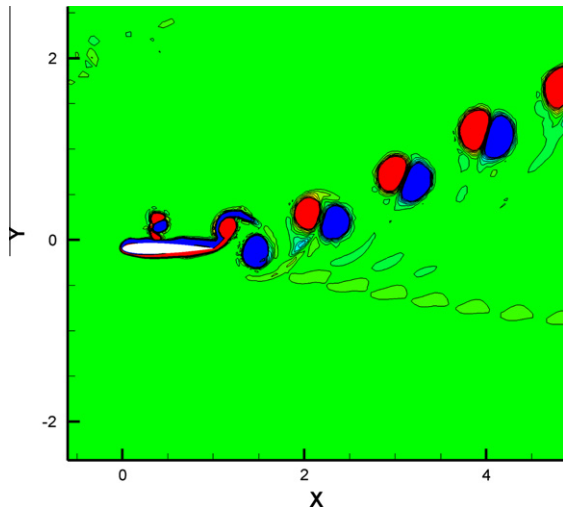


Fig. 16. Vorticity contour predicted on Mesh 1C using the third-order SD method.

4.3.1. The effect of Reynolds number

Four Reynolds numbers (1850, 1000, 500 and 252) are investigated for the fast plunging case. We observe deflected wakes for

all these Reynolds numbers. Interestingly, the angle of deflection decreases as the Reynolds number decreases. Fig. 17 presents vorticity shedding behind the airfoil at different Reynolds numbers. Figures (a), (b), (c) and (d) each contain 12 contour levels within the range of $-6 \leq \omega c/U_\infty \leq 6$. The simulations were performed using the third-order SD method on Mesh 2B for all cases. The time step size $\Delta t U_\infty/c = 2 \times 10^{-5}$ remains the same for all cases.

The variation of Reynolds number results in little change of the lift coefficients as illustrated in Fig. 18a. However, as the Reynolds number decreases, the drag coefficient increases evidently as shown in Fig. 18b. To our knowledge, this is the first report on the dependence of Reynolds numbers for the angle of deflected wakes behind a fast plunging airfoil.

4.4. Viscous flow past a pitching NACA 0012 airfoil

In this section we study viscous flow over a pitching NACA 012 airfoil along its quarter chord axis. The simulations were performed at a much higher Reynolds number than the previous plunging case. In particular, we aim to validate the simulation with existing experiment results of a pitching airfoil, test the solver with increased Reynolds number, and study the lift and drag characteristics of a pitching airfoil.

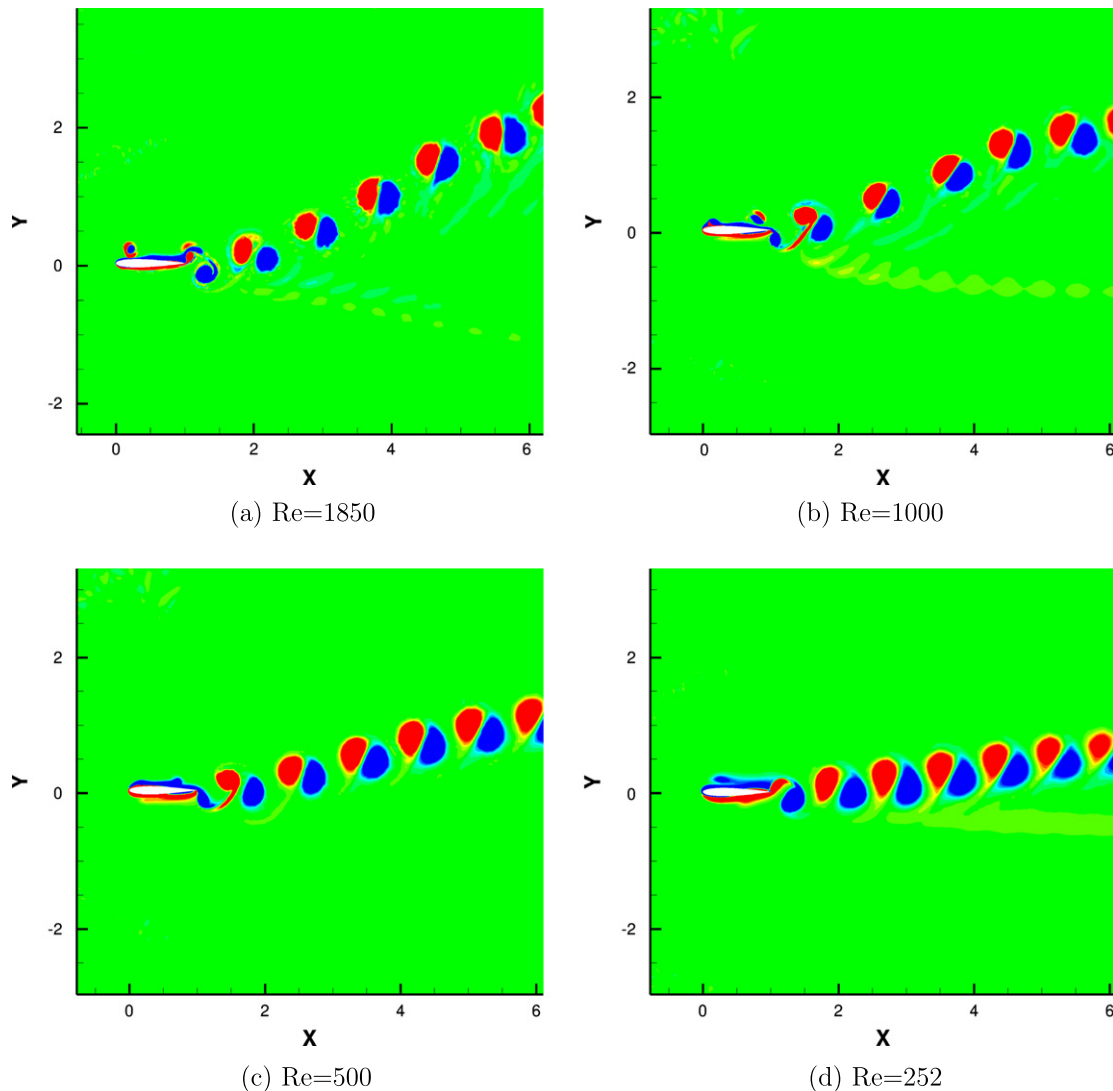


Fig. 17. Vorticity around the fast plunging airfoil at different Reynolds numbers.

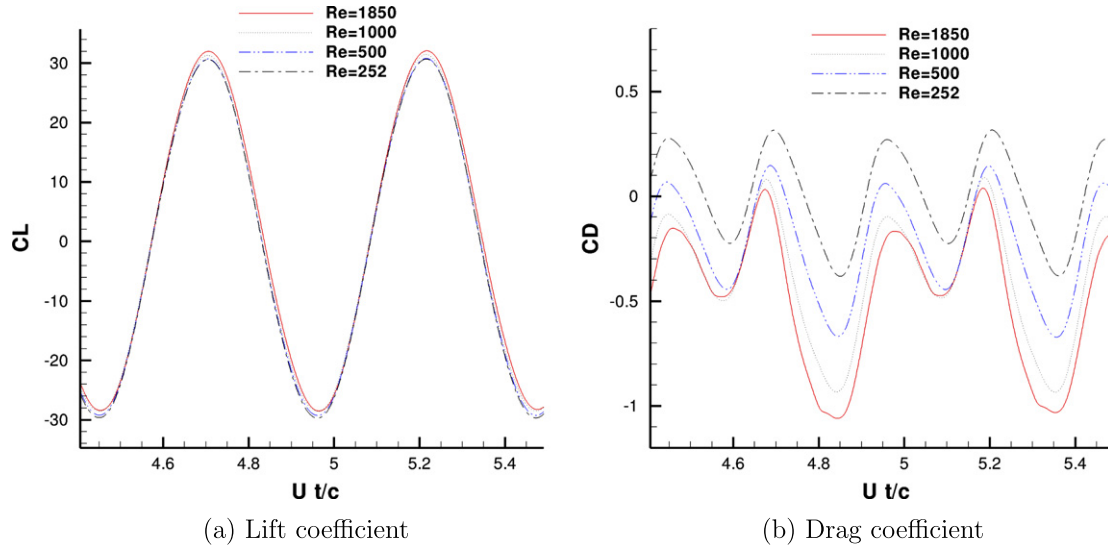


Fig. 18. Lift and drag coefficients predicted for different Reynolds number for the fast plunging case.

4.4.1. Pitching airfoil flow simulation setup

The simulation Reynolds number, based on the airfoil chord length, is $Re = 12,000$. Mesh 1B with 5792 cells is employed for computations of all cases of pitching airfoil. Note that the mesh points are shifted in the streamwise direction so that the quarter chord locates at $(0,0)$. The Reynolds number is chosen according to the experimental study carried out by Koochesfahani [6], in which the vortical patterns behind a pitching NACA0012 airfoil around the quarter chord axis were studied and visualized in a water tunnel. The simulations were computed at a small mach number of $M_\infty = 0.15$, at a reduced frequency k of $2\pi fc / (2u_\infty) = 20.9f$, where f is the pitching frequency. The amplitude of

the sinusoidal pitching motion is denoted A . The airfoil starts with a zero mean angle of attack. Three cases have been computed and compared with the corresponding experimental results. The vortical pattern for each case is illustrated in Figs. 19–21. In order to produce little numerical dissipation, the simulations here were performed with fifth-order SD method.

4.4.2. Pitching airfoil flow patterns

Comparing the vortical patterns, the simulations for the cases with $(A = 4^\circ, k = 0.835)$ and $(A = 2^\circ, k = 6.68)$ produce wakes that are very similar to the experimental visualizations as shown in Figs. 19 and 20. Note that the free-stream flow comes from the

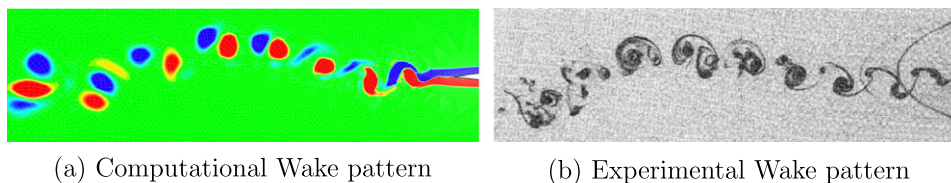


Fig. 19. Vortical pattern for $A = 4^\circ, k = 0.835$.

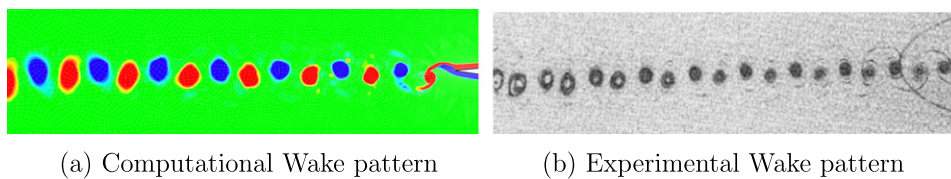


Fig. 20. Vortical pattern for $A = 2^\circ, k = 6.68$.

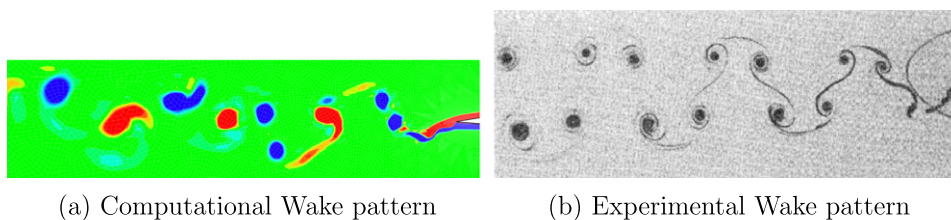


Fig. 21. Vortical pattern for $A = 4^\circ, k = 3.09$.

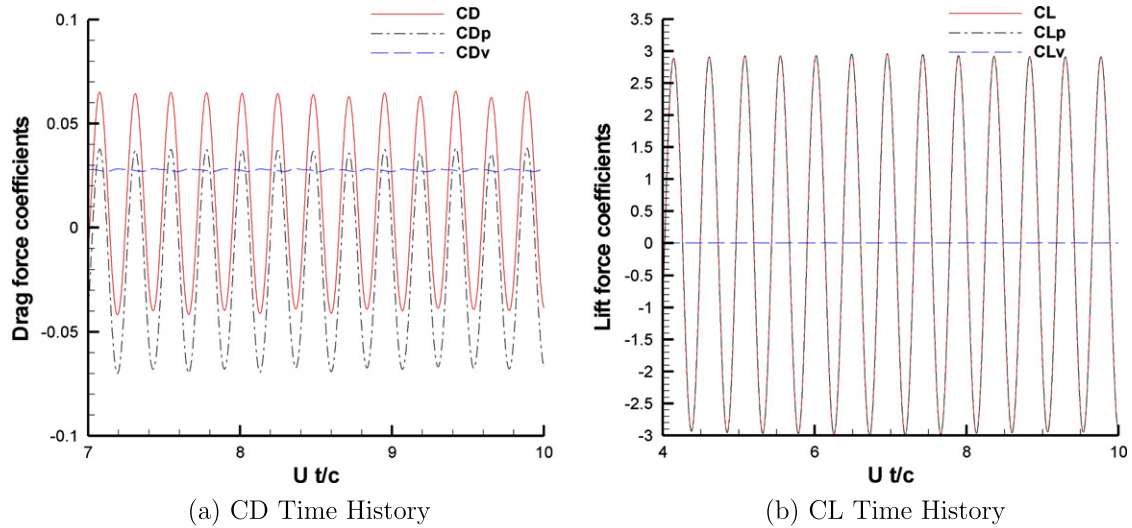


Fig. 22. CD and CL time history for $A = 2^\circ$ and $k = 6.68$.

right side. This is opposite to the previous cases of plunging airfoil. In the first case with ($A = 4^\circ$, $k = 0.835$), the wake assumes a form of undulating vortex sheet. In the later case, an alternating vortex pattern is formed, with the vortices positioned in a nearly straight line, similar to the slow plunging case. For the case with ($A = 4^\circ$, $k = 3.09$), the simulation captures the double-vortex feature, but only in the region about two chords downstream of the airfoil. The vorticity further downstream seems to dissipate and merge into one another, losing the double-vortex feature that is characteristic of this particular pitching frequency and amplitude. It is likely that this special case where two vortices of the same sign are shed on each half-cycle of the oscillation requires a finer mesh downstream of the airfoil, since it occupies a wider flow domain, and has finer features than other cases. Also, the mesh currently used was chosen to be rather unstructured to demonstrate the capability of the solver, hence can introduce more dissipation than otherwise it would. The pitching airfoil considered here has a much higher Reynolds number than the plunging case. In this paper, we only consider 2D simulations. As a result, possible 3D effect is not confirmed. It is worthy of mentioning that Visbal [24] recently studied a plunging airfoil case at a Reynolds number of 10,000

using both 2D and 3D simulations. The 3D effect on lift and drag coefficients is nearly negligible according to his simulations.

4.4.3. Force coefficients time history for $A = 2^\circ$ and $k = 6.68$

As shown in Fig. 22, with the pitching amplitude set to $A = 2^\circ$, and the reduced frequency set to $k = 6.68$, the airfoil produces zero mean lift and generates a small drag force.

The lift coefficient varies sinusoidally with time around zero axis. The average lift acting on the airfoil is zero. The instantaneous lift coefficient is, however, very big, largely due to the contribution from the pressure term, as can be clearly observed from the lift coefficient plot. The skin friction term has negligible contribution to the instantaneous lift force.

While the average lift force is zero, there is a small average drag acting on the airfoil under this condition. The contribution from the skin friction is significant. The skin friction drag coefficient is also nearly constant at a value of $CD_v = 0.0276$. In the contrast, the pressure term has a beneficial mean thrust contribution of $CD_p = -0.015$. This helps to offset the skin friction drag by a large amount, reducing the overall drag acting on the airfoil. The pressure drag term has large instantaneous variations, with half of

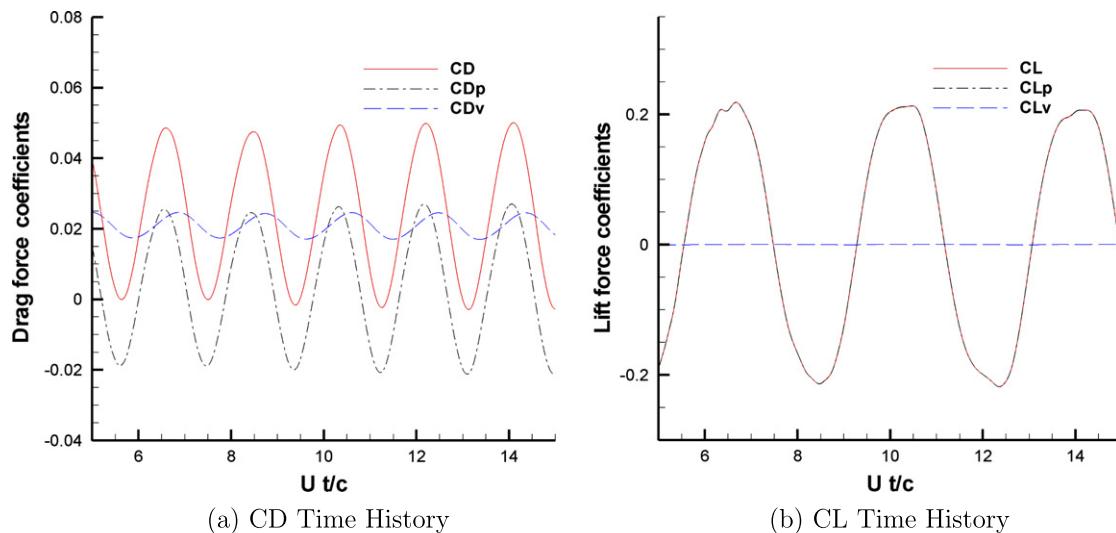


Fig. 23. CD and CL time history for $A = 4^\circ$ and $k = 0.835$.

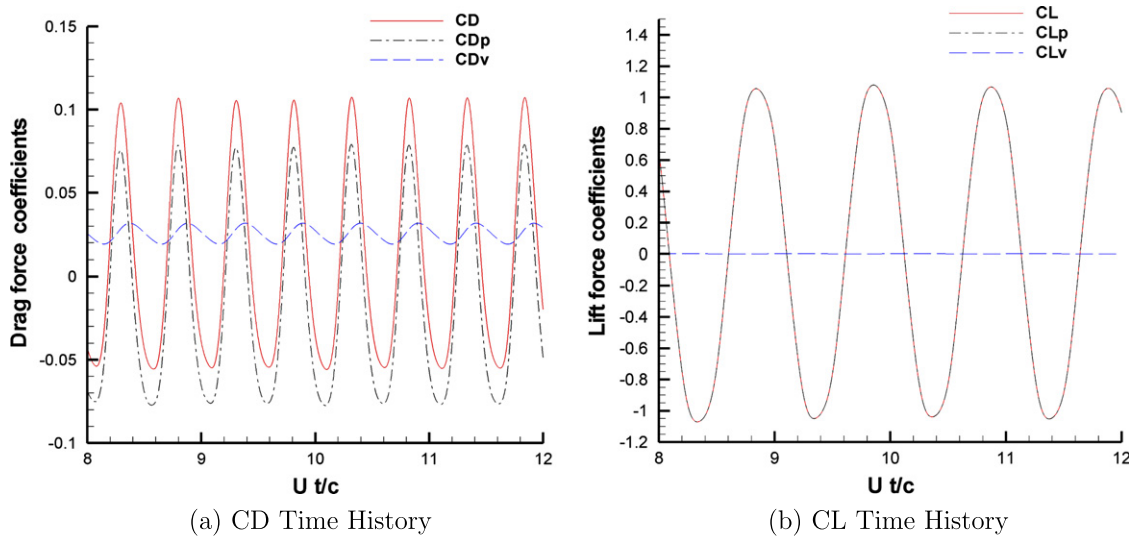


Fig. 24. CD and CL time history for $A = 4^\circ$ and $k = 3.09$.

Table 2
Drag coefficients for various pitching frequencies and amplitudes.

A	K	CD_p	CD_v	CD_t	A	K	CD_p	CD_v	CD_t
	0	0	0.0254	0.0254		0	0	0.0254	0.0254
2	5.01	-0.0039	0.0253	0.0214	4	0.835	0.0045	0.0234	0.0253
	6.68	-0.0172	0.0276	0.0104		3.09	-0.0139	0.0255	0.0115

the pitching cycle producing thrust, and the other half generating drag.

4.4.4. Force coefficients time history for $A = 4^\circ$ and $k = 0.835$

As shown in Fig. 23, with the pitching amplitude set to $A = 4^\circ$, and the reduced frequency set to $k = 0.835$, the airfoil produces zero mean lift and generates a drag force that is larger than the previous case.

The lift coefficient time history is very similar to the previous case, with large instantaneous but zero average value.

The entire drag coefficient curve stays above the zero axis. Hence the airfoil experiences drag at all time. The contribution from the skin friction term is almost the same as the previous case, with $CD_v = 0.0234$. The pressure term, however, has zero mean contribution to the drag. The mean overall drag force is entirely due to skin friction.

4.4.5. Force coefficients time history for $A = 4^\circ$ and $k = 3.09$

As shown in Fig. 24, with the pitching amplitude set to $A = 4^\circ$, and the reduced frequency set to $k = 3.09$, the airfoil again produces zero mean lift, but a smaller drag force than the previous case.

Again, no mean lift force is produced, and the instantaneous force remains large.

The skin friction remains at about $CD_v = 0.0255$. The pressure term is thrust producing with an average $CD_p = -0.0139$. This helps to reduce the overall mean drag force.

4.4.6. Variation of drag coefficient with reduced frequency

Three additional cases have been computed to produce the following curves showing the variation of drag coefficients with reduced frequencies for different pitching amplitudes. The mean CD values for all the cases are also tabulated in Table 2.

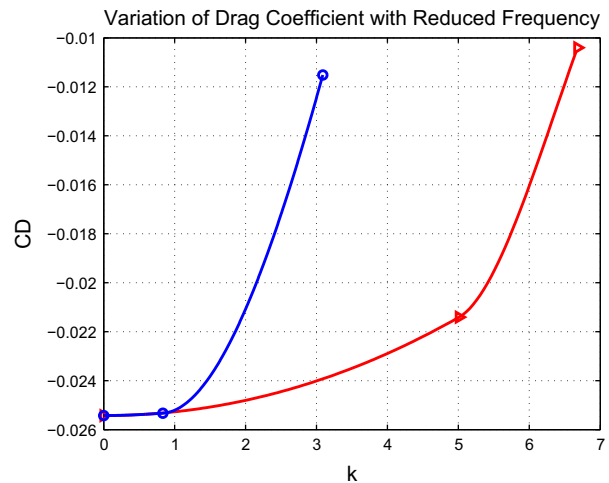


Fig. 25. Variation of drag coefficient with reduced frequency for amplitude = 2° (triangle) and amplitude = 4° (circle).

From the previous section, we note that, by pitching faster, the pressure term becomes thrust producing while the skin friction term remains roughly unaltered, leading to an overall reduction in drag experienced by the airfoil. Both curves shown in Fig. 25 demonstrate the beneficial effect of increasing pitching frequency. We also observe that this effect is more pronounced for higher pitching amplitude.

5. Conclusions

The spectral difference method is robust and accurate. Both third and fourth-order SD simulations of unsteady flow past a

plunging airfoil confirm that the vortex shedding pattern becomes asymmetric at a sufficiently high frequency. The fourth-order SD method both captures this effect and also reveal a fine structure that closely replicates the experimental photographs. It is found that the vortex shedding frequencies of these plunging airfoils are equivalent to the plunging frequencies. *The angle of deflected wake increases with the Reynolds number. Conversely, the increase of Reynolds number from 252 to 1850 results in decreases of the drag coefficient.*

Our predictions for the pitching airfoil also achieved excellent agreements with experimental data. Comparison between our high-order SD simulations and other inviscid flow solvers confirms that it is necessary to solve a full set of Navier–Stokes equations in order to predict accurately both lift and drag characteristics for oscillating airfoils.

The SD method could enable high-order accurate simulations of unsteady flow past flapping MAVs. Our planned future work is to apply this technique for predictions of unsteady flow past oscillating wings with combined plunging and pitching motion.

Acknowledgement

The authors would like to thank the grant supports from NSF monitored by Dr. Leland Jameson with award number 0708071 and AFOSR monitored by Dr. Fariba Fahroo with Grant No. FA9550-07-1-0195.

References

- [1] Bassi F, Rebay S. High-order accurate discontinuous finite element solution of the 2d euler equations. *J Comput Phys* 1997;138:251–85.
- [2] Heathcote S, Gursul I. Jet switching phenomenon for a periodically plunging airfoil. *Phys Fluids* 2007;19. 027104–1–12.
- [3] Huynh H. A flux reconstruction approach to high-order schemes including discontinuous galerkin methods. *AIAA paper AIAA-2007-4079*, 2007.
- [4] Jones KD, Dohring CM, Platzer MF. Experimental and computational investigation of the Knoller–Betz effect. *AIAA J* 1998;36:780–3.
- [5] Kinsey T, Dumas G. Parametric study of an oscillating airfoil in a power-extraction regime. *AIAA J* 2008;46:1318–30.
- [6] Koochesfahani MM. Vortical patterns in the wake of an oscillating airfoil. *AIAA J* 1989;27:1200–5.
- [7] Kopriva DA, Kollias JH. A conservative staggered-grid chebyshev multidomain method for compressible flows. *J Comput Phys* 1996;125:244–61.
- [8] Lewin GC, Haj-Hariri H. Modelling thrust generation of a two-dimensional heaving airfoil in a viscous flow. *J Fluid Mech* 2003;339:362. 027104–1–12.
- [9] Liang C, Jameson A, Wang ZJ. Spectral difference method for two-dimensional compressible flow on unstructured grids with mixed elements. *J Comput Phys* 2009;228:2847–58.
- [10] Liang C, Kannan R, Wang ZJ. A p-multigrid spectral difference method with explicit and implicit smoothers on unstructured triangular grids. *Comput Fluids* 2009;38:254–65.
- [11] Liang C, Premasathan S, Jameson A. High-order accurate simulation of flow past two side-by-side cylinders with spectral difference method. *Comput Struct* 2009;87:812–27.
- [12] Liu Y, Vinokur M, Wang ZJ. Spectral difference method for unstructured grids I. Basic formulation. *J Comput Phys* 2006;216:780–801.
- [13] Liu Y, Vinokur M, Wang ZJ. Spectral (finite) volume method for conservation laws on unstructured grids V. Extension to three-dimensional systems. *J Comput Phys* 2006;212:454–72.
- [14] McKinney W, DeLaurier J. Wingmill: an oscillating-wing windmill. *J Energy* 1981;5:109–15.
- [15] Michalak C, Ollivier-Gooch C. Unstructured high-order accurate finite-volume solutions of the Navier–Stokes equations. *AIAA paper AIAA-2009-954*, 2009.
- [16] Morton SA, Melville RB, Visbal MR. Accuracy and coupling issues of aeroelastic Navier–Stokes solutions on deforming meshes. *J Aircraft* 1998;35:798–805.
- [17] Persson PO, Bonet J, Peraire J. Discontinuous galerkin solution of the Navier–Stokes equations on deformable domains. *Comput Methods Appl Mech Eng* 2009;198:1585–95.
- [18] Platzer MF, Ashraf MA, Young J, Lai JCS. Development of a new oscillating-wing wind and hydropower generator. *AIAA paper AIAA-2009-1211*, 2009.
- [19] Roe PL. Approximate riemann solvers, parameter vectors and difference schemes. *J Comput Phys* 1981;43:357–72.
- [20] Rusanov VV. Calculation of interaction of non-steady shock waves with obstacles. *J Comput Math Phys USSR* 1961;1:261–79.
- [21] Spiteri RJ, Ruuth SJ. A new class of optimal high-order strong-stability-preserving time discretization methods. *SIAM J Numer Anal* 2002;40:469–91.
- [22] Sun Y, Wang ZJ, Liu Y. High-order multidomain spectral difference method for the Navier–Stokes equations on unstructured hexahedral grids. *Commun Comput Phys* 2007;2:310–33.
- [23] Van den Abeele K, Lacor C, Wang ZJ. On the stability and accuracy of the spectral difference method. *J Sci Comput* 2008;37:162–88.
- [24] Visbal M. High-fidelity simulation of transitional flows past a plunging airfoil. *AIAA J* 2009;47:2685–97.
- [25] Wang Z, Liu Y, May G, Jameson A. Spectral difference method for unstructured grids II. Extension to the Euler equations. *J Sci Comput* 2007;32:45–71.
- [26] Wang ZJ, Liu Y. Extension of the spectral volume method to high-order boundary representation. *J Comput Phys* 2006;211:154–78.